Supplemental Document

OPTICA

High-throughput multimodal wide-field Fourier-transform Raman microscope: supplement

B. Ardini,[1] A. Bassi,[1] A. Candeo,[1] A. Genco,[1] C. Trovatello,[2] F. Liu,[3,4] X. Zhu,[3] G. Valentini,[1,5] G. Cerullo,[1,5] R. Vanna,[5,6] and C. Manzoni[5,*]

[1] *Dipartimento di Fisica, Politecnico di Milano, Piazza Leonardo da Vinci 32, I-20133 Milano, Italy*
[2] *Department of Mechanical Engineering, Columbia University, New York, New York 10027, USA*
[3] *Department of Chemistry, Columbia University, New York, New York 10027, USA*
[4] *Department of Chemistry, Stanford University, Stanford, California 94305, USA*
[5] *Istituto di Fotonica e Nanotecnologie, IFN-CNR, Piazza Leonardo da Vinci 32, I-20133 Milano, Italy*
[6] *renzo.vanna@cnr.it*
[*] *cristianangelo.manzoni@cnr.it*

Supplement DOI: https://doi.org/10.6084/m9.figshare.22728770

Parent Article DOI: https://doi.org/10.1364/OPTICA.488860

A high-throughput fluorescence-free widefield Fourier-transform Raman microscope: Supporting Information

B. Ardini[1], A. Bassi[1], A. Candeo[1], R. Vanna[2], A. Genco[1], C. Trovatello[3], F. Liu[4,#], X. Zhu[4], G. Valentini[1,2], G. Cerullo[1,2] and C. Manzoni[2,*]

[1]*Dipartimento di Fisica, Politecnico di Milano, Piazza Leonardo da Vinci 32, I-20133 Milano, Italy*
[2]*Istituto di Fotonica e Nanotecnologie, IFN-CNR, Piazza Leonardo da Vinci 32, I-20133 Milano, Italy*
[3]*Department of Mechanical Engineering, Columbia University, NY, 10027, USA*
[4]*Department of Chemistry, Columbia University, NY, 10027, USA*
[#]*Department of Chemistry, Stanford University, Stanford, CA, 94305, United States*
[*]*cristianangelo.manzoni@cnr.it, renzo.vanna@cnr.it*

1. Characterization of Top-hat illumination

In order to characterize the top-hat illumination of our system, we measured the emission of a fluorescent thin dye film after exciting with the laser. The dye was deposited on an optically-grade silver mirror to reduce light scattering from the substrate. Narrowband excitation was provided by a frequency doubled Nd:YAG laser (λ = 532 nm), coupled to the microscope by the optical fiber, as described in Section 2, main text. The fiber diameter was 400 μm and the objective had 10× magnification.

The spot characterization is displayed in Fig. 1. Panel (a) shows the fluorescence image;

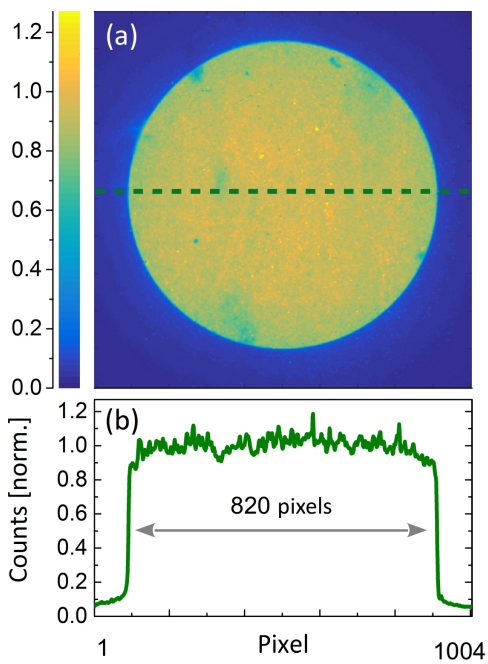

Fig. 1. Characterization of the microscope laser illumination system. (a) Fluorescence intensity from the thin dye film placed at the sample plane. (b) Cross-section corresponding to the green-dashed line of the intensity map of panel (a).

since fluorescence is proportional to the illumination intensity, the map conveys the shape and distribution of the illumination field at the sample plane. It has a diameter proportional to the fiber diameter; a cross section of the image (dash-green line) is shown in panel (c): the intensity is mostly flat over the entire circular surface, the small intensity fluctuations being attributed to inhomogeneities of the dye concentration. The illumination diameter covers 82% of the field of view (FOV) width. Since both the illumination light and the image propagate through the same objective, the ratio of 82% holds for any magnification. Finally, the small background is attributed to scattering of the illumination light and of the fluorescence.

2. The TWINS interferometer

Our TWINS interferometer is based on birefringence. A birefringent crystal is characterized by a privileged direction named optical axis. When a light waveform propagates in such material, ordinary polarization (*i.e.*, normal to the optical axis) and extraordinary polarization (*i.e.*, parallel to the optical axis) experience two different refractive indices (n_o and n_e respectively) and hence they travel with different velocities, thus accumulating a relative delay proportional to the propagation length. By varying the material thickness, an arbitrary delay can be imposed on the two polarization components. Both replicas follow the same optical path: as a consequence, they do not accumulate relative path-length fluctuations and their delay is fixed with unprecedented stability.

This concept is employed in our interferometer, which is sketched in the inset of Fig. 1, main text; it consists of two blocks, B_1 and B_2, of the same birefringent material. Their optical axes are mutually crossed, so that they introduce delays with opposite signs. Since block B_1 consists of two wedges with an overall variable thickness, the delay accumulated by the two replicas after the blocks is adjusted by moving one of the wedges. The maximum delay T_{max} of the interferometer depends on three parameters: the crystal birefringence $\Delta n = n_o - n_e$, the wedge apex angle α and the maximum translation length L. Table 1 lists the optical properties of the most common uniaxial birefringent materials which are transparent in the visible. Following this table, for RS applications YVO_4 offers the best compromise between transparency range, birefringence and the refractive index strength.

Table 1. Uniaxial birefringent crystal with transparency in the visible spectral range. The crystals are listed in order of decreasing birefringence. Positive (negative) uniaxial crystals have $\Delta n > 0$ ($\Delta n < 0$).

Crystal	$\Delta n = n_o - n_e$	$n_o(\lambda = 0.63\ \mu m)$	Transparency (μm)
TiO_2	+0.282	2.583	0.5-4.5
YVO_4	+0.222	1.9929	0.4-5
$CaCO_3$	-0.1705	1.6557	0.35-2.3
α-BBO	-0.139	1.6707	0.189-3.5
$PbMoO_4$	-0.124	2.386	0.42-5.5
TeO_2	-0.118	2.260	0.35-5
$LiNbO_3$	-0.086	2.286	0.4-5

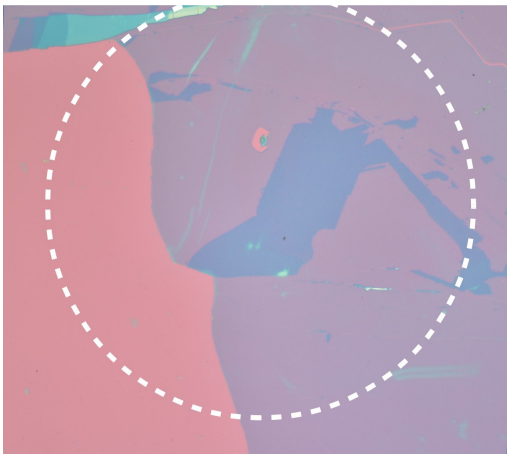

Fig. 2. Reflectivity image of the sample under visible illumination, collected with an optical microscope equipped with an RGB camera. The white dashed circle denotes the area that is illuminated by the laser used for the acquisition of Raman and fluorescence images. The image has been collected with a 10× objective.

3. Sample preparation

3.1. PS/PMMA beads

Aqueous suspensions of polystyrene (PS) microparticles (72986-5ML-F, Merck KGaA, Darmstadt, Germaniy) and of poly(methacrylic acid) (PMMA) microparticles (90515-5ML-F, Merck KGaA, Darmstadt, Germaniy), of $\sim 8\,\mu$m and $\sim 10\,\mu$m diameter, respectively, were diluted 100 times and mixed 1:1 in water (1 mL). $2\,\mu$l of this suspension were deposited onto mirrored stainless steel slides (Renishaw plc, Wotton-under-Edge, UK) and air dried for 30 minutes.

3.2. WSe_2 multilayer

The monolayer WSe_2 sample is prepared from the bulk WSe_2 crystal (HQ Graphene) by using a gold-assisted large area exfoliation technique [1]. A layer of gold is evaporated on a clean Si wafer. A piece of thermal release tape is used to tear Au off the Si and expose clean and flat Au surface. The Au surface is pressed on top of the cleaved WSe_2 bulk crystal. When the thermal release tape/ Au layer is taken off the WSe_2 crystal surface, it carries a large piece of WSe_2 monolayer on the contact surface. The thermal release tape/Au/monolayer is then transferred onto a reflective 285 nm SiO_2/Si wafer substrate. The thermal release tape is removed by heating up to 130 °C, and the residues are cleaned with subsequent acetone cleaning and O2 plasma treatment. Finally, we dissolve the gold layer with a gold etchant solution (KI and I_2 in deionized water) [1]. The reflectivity image of the sample is shown in Fig. 2.

4. Interferograms sampling period

For a fixed delay-scan range $T = |T_2 - T_1|$, the interferogram sampling period T_s determines the total acquisition time and the spectrum SNR. Generally, the SNR of a measurement can be improved by averaging N acquisitions, since uncorrelated noise reduces in proportion to $\sqrt{N}$. In FT spectroscopy, however, one can adopt a different approach: instead of averaging N spectra [2], the same effect is obtained by taking only one scan with increased number of samples, *i.e.* reducing the sampling period T_s by a factor of N [3]. As this increases the overall measurement time, the optimal T_s is a trade-off between scanning time and SNR increase.

If noise is not an issue, one may opt for large sampling steps in order to reduce the measurement time. However, large T_s may lead to spectral aliasing and corresponding information loss, and an upper constraint is posed. This limit depends on the highest ($\nu_{\max}$) and lowest ($\nu_{\min}$) frequency components of the measured spectrum. The most common and restrictive sampling criterion is the Nyquist-Shannon (NS) limit, which assumes $\nu_{\min} = 0$, and hence imposes $T_s < 1/(2\nu_{\max})$; however this limit can be overcome if $\nu_{\min} \neq 0$. In our experiment we exploited this feature thanks to the use of a short-pass filter in the detection path, to narrow the detection spectral bandwidth around the expected Raman-shift range. Thanks to this property, we could use larger values of T_s, enabling a drastic reduction of the acquisition time with respect to the NS limit, without information loss.

5. Interferograms apodization

The apodization is a necessary operation before taking the FT to retrieve the spectrum. It avoids abrupt cutting of the interferogram at its edges, which would otherwise end up in spectral artifacts in the form of side-bands, and consists in the multiplication of the interferogram by a proper windowing function [4]. There is a variety of apodization functions, each of them characterized by the amount of residual side-bands and loss of resolution. The simplest one is the rectangle, which is equivalent to having no apodization. A detailed catalog of such windowing functions can be found in [5, 6]. In our FT-HSM, for both Raman and fluorescence measurements we apply the Happ-Genzel (Hamming) window, which is a good compromise between spectral broadening and side-lobes suppression. With this function, the spectral peaks broaden by less than $\sim 50\,\%$ with respect to the non-apodized case [5]; the side-lobes level is $\sim 20\,\mathrm{dB}$ lower than the main peak, well below the typical noise level in Raman measurements ($\sim -10\,\mathrm{dB}$) and comparable to the residual spectral sidebands determined by the delay axis error (see Section 8)

6. Computing time and data volume

The hyperspectral cube is generated by taking the FT at each image pixel; the computation time depends on the number of the temporal and the frequency samples, and on the number of pixels. As an example, with a standard commercial PC (RAM: 16GB, CPU: Intel i7 or similar), the generation of the hypercube of an image with 100k pixels, 800 samples and 1500 spectral frequencies requires 1 min,which is negligible with respect to the time required to acquire the RS image; the resulting datacube has a volume of 400MB.

6.1. WSe_2 multimodal measurements acquisition parameters

Table 2 lists the parameters used in the fluorescence and Raman measurements of the multilayer WSe_2 sample.

7. Frequency calibration

The frequency calibration of the TWINS spectrometer has been described in [7] and [8] . The procedure consists in measuring spectra of light sources with known peaks (e.g. monochromatic laser lines, light transmitted by narrow bandpass filters, etc. . .) and associating them to the corresponding features provided by the TWINS interferometer [9, 10]: the calibration curve is finally obtained by interpolating the data points. We have calibrated our interferometer by measuring the Raman peaks of uniform pure samples: Polystyrene (PS), Calcium Carbonate ($CaCO_3$) and Whitlockite ($Ca_9(MgFe)(PO_4)_6PO_3OH$). Their Raman peaks have been retrieved by averaging the spectra of all the excited pixels. A quadratic fit of the retrieved data points provides a calibration curve with 23-cm^{-1} norm of residuals.

Table 2. Acquisition parameters for the multimodal imaging of WSe_2. Exposure is the integration time of each frame, while Acquisition time is the time required to acquire the whole dataset. *Acquisition time* and *Intensity* are calculated from the corresponding values of the table.

	Fluorescence	Raman
Scan range [fs]	-65.50 → 65.50	34 → 2524
Number of frames	200	3064
Binning	4×4	6×6
Number of pixels	62500	27800
Exposure [sec]	4	2.3
Pump Power [mW]	2	200
Acquisition time [min]	14	165
Intensity [W/cm^2]	2.5	250

8. Correction of the delay axis

Errors of the delay axis are detrimental in FT spectroscopy as they introduce artifacts in the retrieved spectra. Errors in the delay arise from the deviations between the expected and the true motor positioning [7]. Such artifacts are mainly in the form of sidebands around the spectral peaks, which could heavily mislead the interpretation of Raman spectra. For this reason, it is important to calibrate the effective delay-axis, and correct for deviations. In [7] we presented a delay correction procedure that successfully suppressed almost completely the spectral sidebands to the −30 dB level. In that case the delay scan was 570 fs long (10 −mm motor scan, with wedges made of α-BBO and tip angle of $\alpha = 7^o$). However this correction method is not effective for the current interferometer (2000 −fs−delay scan, 15.3 −mm motor scan, YVO_4 wedges and tip angle of $\alpha = 10^o$). For this reason we have formulated a novel algorithm, which is based on frequency demodulation. The technique is based on the acquisition of the interferogram of a monochromatic laser, which corresponds to a cosinusoid function of the delay τ oscillating at the frequency ν. In the presence of positioning errors of the motor, the sample attributed to τ is instead collected at $\tau + \Delta\tau_{\text{err}}(\tau)$, which corresponds to an additional phase term $\phi_{\text{err}} = 2\pi\nu \cdot \Delta\tau_{\text{err}}(\tau)$. Hence the sampled interferogram $g(\tau)$ is:

$$g(\tau) = \frac{1}{2}e^{i[2\pi\nu\tau+\phi_{\text{err}}(\tau)]} + \frac{1}{2}e^{-i[2\pi\nu\tau+\phi_{\text{err}}(\tau)]} \tag{1}$$

From the sampled interferogram, we need now to extract ϕ_{err} and the corresponding $\Delta\tau_{\text{err}}(\tau)$ attributed to the delay line. One method to extract this parameter is through multiplication of the time trace by $e^{-i2\pi\nu\tau}$, which gives:

$$g(\tau) \cdot e^{-i2\pi\nu\tau} = \frac{1}{2}e^{i\phi_{\text{err}}(\tau)} + \frac{1}{2}e^{-i[2\cdot 2\pi\nu\tau+\phi_{\text{err}}(\tau)]} \tag{2}$$

This is a fast oscillation at frequency 2ν overlapped to a much slower oscillation term due to $\phi_{\text{err}}(\tau)$. The fast oscillation is suppressed by applying a numeric low-pass filter in the Fourier domain and subsequently by back-transformation into the τ domain. The delay error is retrieved by extracting the phase of the remaining term, $G(\tau) = \frac{1}{2}e^{i\phi_{\text{err}}(\tau)}$, as follows:

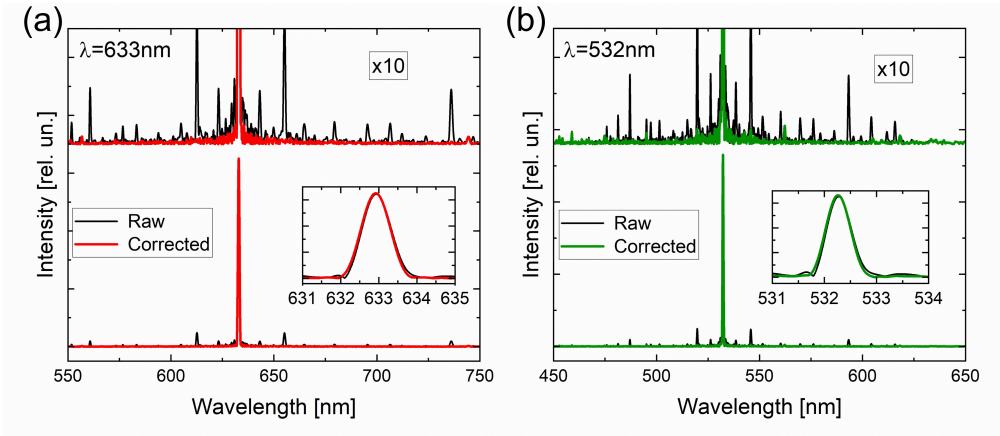

Fig. 3. Spectra before (Raw) and after (Corrected) the delay axis correction for (a) HeNe (λ = 633 nm) and (b) frequency doubled Nd:YAG (λ = 532 nm) laser lines. The insets show the detail of the laser peaks; in the upper part the same spectra have been reported with ×10 multiplication for clarity.

.

$$\Delta\tau_{\mathrm{err}}(\tau) = \frac{\arg[G(\tau)]}{2\pi\nu} = \frac{\phi_{\mathrm{err}}(\tau)}{2\pi\nu} \tag{3}$$

To retrieve the delay error of our stepper motor (Physik Instrumente M-112.12S1), we measured the light from a He:Ne laser (λ = 632.8 nm) in reflection; then we applied our method to the average interferogram from the pixels inside the illuminated area of the FOV. Figure 3(a) shows the spectra of the He:Ne laser obtained from the FT of the interferogram before (black line) and after (red line) the delay correction. To test the effectiveness of the method, we applied the retrieved delay correction $\Delta\tau_{\mathrm{err}}(\tau)$ to the interferogram of our Raman illumination (a frequency doubled Nd:YAG laser, λ = 532 nm); note that the correction was not performed during the acquisition, but was applied to the time axis right before taking the FT. The retrieved spectra are shown in Figure 3(b), where the black line is the FT of the uncorrected time trace, while the green line is obtained after the correction of the time axis. The spectra show that the correction obtained from the He:Ne laser is also effective to correct the trace of the λ = 532 nm light, since it almost eliminates the side lobes and does not affect the spectral peaks (see insets in Figure 3). This also confirms that the positioning error of the translation stage is mostly systematic, and it is not required to perform the delay calibration at any measurement run.

As the correction does not completely remove all the sidebands artifacts effectively, a complete filtering of the laser illumination in Raman measurement with FT-HSM is fundamental in order to avoid the appearance of artifact peaks in the Raman spectrum, which may have intensities comparable to the modes of the samples.

9. Comparison with Standard Raman spectroscopy measurements

Standard spontaneous Raman measurements were performed using a home-built Raman microscope. The illumination light, provided by a continuous-wave diode laser centered at 660 nm (Cobolt AB, Flamenco, Solna, Sweden) is filtered using a shortpass filter (FESH0750, ThorLabs, Newton, NJ, USA), to remove possible spurious emissions, expanded by a beam expander (GBE05-B, ThorLabs, Newton, NJ, USA) and then reflected by a single-edge dichroic beamsplitter (Di03-R660-t1-25x36, Semrock, Inc., Rochester, NY, USA) aiming to separate illumination

and emitted Raman photons. The light enters the back port of a commercial inverted microscope (IX73, Olympus Europa SE & Co. KG, Hamburg, Germany) and is focused on the sample using a dry/air 50x objective (MPLFLN50X 20x/0.80 NA, Olympus). The scattered light is collected by the same objective and transmitted by the dichroic beamsplitter. A long-pass (664 nm) edge filter (LP02-664RU-25, Semrock, Inc.) is then used to remove the residual laser light and the scattered light is focused by a lens (f = 35 mm, AC254-035-B-ML, ThorLabs, Newton, NJ, USA) on the entrance slit of a spectrometer (Isoplane160, Princeton instruments, Trenton, NJ, USA) equipped with a silver coated grating of 660 gr/mm and connected to a front illuminated CCD (PIXIS256F, Princeton Instruments, Trenton, NJ, USA). The wavenumber calibration was performed using toluene and a ArHg lamp (AvaLight CAL-MINI, Avantes, Apeldorn, The Netherlands) as references. Intensity calibration was performed using a calibrated white lamp (AvaLight HAL-CAL-MINI, Avantes, Apeldorn, The Netherlands). The illumination power used to collect spectra from PS and PMMA beads was 50mW and the spectra were collected by integrating the signal for 5s, averaging 5 acquisitions. Spectral data were only calibrated and corrected for eventual cosmic rays, without performing further processing.

The comparison in Figure 4 shows a good agreement between the spectra obtained from the HSM measurement (by exploiting two different analysis approaches) and the ones measured with the standard home-built Raman microscope.

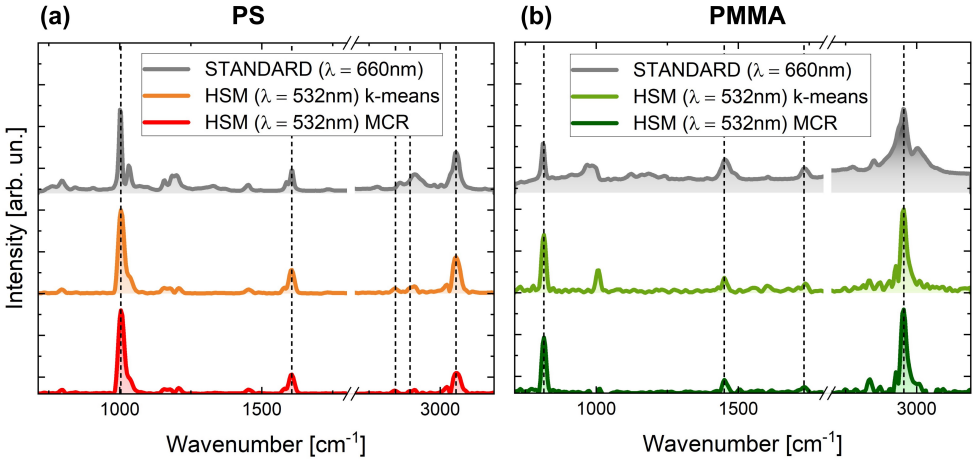

Fig. 4. Comparison between spectra obtained with standard Raman spectrometer (in grey) and with mini-batch k-means and MCR analysis on Raman HSM measurements (in color) (a) for PS and (b) for PMMA beads. The dashed lines highlight the characteristic Raman peaks of the two types of beads.

.

References

1. F. Liu, W. Wu, Y. Bai, S. H. Chae, Q. Li, J. Wang, J. Hone, and X.-Y. Zhu, "Disassembling 2d van der waals crystals into macroscopic monolayers and reassembling into artificial lattices," Science **367**, 903–906 (2020).
2. W. Perkins, "Fourier transform-infrared spectroscopy: Part l. instrumentation," J. Chem. Educ. **63**, A5 (1986).
3. H. M. Pickett and H. L. Strauss, "Signal-to-noise ratio in fourier transform spectrometry," Anal. Chem. **44**, 265–270 (1972).
4. R. Bell, *Introductory Fourier transform spectroscopy* (Elsevier, 2012).
5. W. Herres and J. Gronholz, "Understanding ft-ir data processing. part 1: Data acquisition and fourier transformation," Comput. Appl. Lab. **2**, 216–220 (1984).
6. F. J. Harris, "On the use of windows for harmonic analysis with the discrete fourier transform," Proc. IEEE **66**, 51–83 (1978).

7. A. Perri, B. N. de Faria, D. T. Ferreira, D. Comelli, G. Valentini, F. Preda, D. Polli, A. De Paula, G. Cerullo, and C. Manzoni, "Hyperspectral imaging with a TWINS birefringent interferometer," Opt. Express **27**, 15956–15967 (2019).
8. A. Oriana, J. Réhault, F. Preda, D. Polli, and G. Cerullo, "Scanning fourier transform spectrometer in the visible range based on birefringent wedges," J. Opt. Soc. Am. A **33**, 1415–1420 (2016).
9. D. Brida, C. Manzoni, and G. Cerullo, "Phase-locked pulses for two-dimensional spectroscopy by a birefringent delay line," Opt. Lett. **37**, 3027–3029 (2012).
10. J. Réhault, M. Maiuri, A. Oriana, and G. Cerullo, "Two-dimensional electronic spectroscopy with birefringent wedges," Rev. Sci. Instruments **85**, 123107 (2014).